

Iron silicides grown by solid phase epitaxy on a Si(111) surface: Schematic phase diagramK. Kataoka,^{1,*} K. Hattori,^{1,2,†} Y. Miyatake,³ and H. Daimon^{1,2}¹*Graduate School of Materials Science, Nara Institute of Science and Technology (NAIST), Ikoma, Nara 630-0192, Japan*²*CREST-JST, Kawaguchi, Saitama 332-0012, Japan*³*UNISOKU Co., Ltd., Hirakata, Osaka 573-0131, Japan*

(Received 4 October 2005; revised manuscript received 21 June 2006; published 4 October 2006)

We have determined the schematic phase diagram in detail with high reliability for Fe silicides grown by solid phase epitaxy (SPE) on a Si(111)7×7 surface at wide Fe coverage (0.2–56 monolayers) and subsequent annealing temperatures from 300 to 800 °C. In the SPE growth, δ -7×7, 1×1, bcc-Fe(111)1×1, 2×2, $c(8\times4)$, 3D-2×2 (α -FeSi₂), $\sqrt{3}\times\sqrt{3}$ -R30°, β -FeSi₂, and fine polycrystalline phases are formed on the Si(111) surface depending on Fe coverage and annealing temperature. We have characterized the surface periodic structures and morphologies of all the above Fe silicide phases using low-energy electron diffraction and scanning tunneling microscopy. Reflection high-energy electron diffraction also has been used to determine three-dimensional structures. Based on the overall view regarding the formations and changes of Fe silicide phases on a Si(111) surface, we discuss the growth mechanisms.

DOI: [10.1103/PhysRevB.74.155406](https://doi.org/10.1103/PhysRevB.74.155406)

PACS number(s): 68.55.–a, 68.37.Ef, 68.47.Fg, 61.14.Hg

I. INTRODUCTION

The structure and electronic properties of Fe silicides grown on a Si surface have been widely studied for applications to Si-based device technology. In particular, the semiconducting β -FeSi₂ epitaxial phase grown on a Si surface has attracted much attention as a candidate for optoelectronic devices^{1,2} because it has a band gap of ~0.8–0.9 eV corresponding to the adsorption minimum of silica optical fiber. The electric properties,^{3,4} magnetic properties,^{5–7} and gas reactions^{8,9} of various Fe silicides on Si also have been investigated. However, it is difficult to control the crystallinity and morphology of thin epitaxial phases depending strongly on the growth conditions, which seriously affect device properties. A systematic guideline to understand the Fe silicide growth on Si surfaces has not been shown yet. Therefore, systematic characterizations of the structure and morphology for the thin epitaxial Fe silicide phases provide important information for the improvement of the materials quality.

The Fe-Si binary bulk system shows several stable silicide structures as a function of stoichiometry and temperature,^{10–12} such as the cubic ϵ -FeSi (B20), the tetragonal α -FeSi₂, the orthorhombic β -FeSi₂, and other structures. In the Si(111)-Fe system, however, several metastable epitaxial silicides [1×1 , 2×2 , and $c(8\times4)$ phases], which are unstable in bulk, can be formed under the strain from Si(111) substrates in addition to the bulk phases. The FeSi with a CsCl (B2) structure has been proposed for the 1×1 phase.^{13–17} For the 2×2 phase, γ -FeSi₂ with a CaF₂(C1) structure^{14,18–22} and FeSi_{1+x} ($0\leq x\leq 1$) with a defect-CsCl structure derived from the CsCl structure with Fe vacancies distributed in a random fashion^{15,21–24} have been proposed. Recently, a $c(8\times4)$ surface structure made of the 2×2 array has been observed,²⁵ and a structure derived from the CsCl structure has been discussed.²⁶ Moreover, the formation of a $\sqrt{3}\times\sqrt{3}$ -R30° structure has been reported and explained as the epitaxy of bulk ϵ -FeSi.^{18,20,22,27,28} Also epitaxial growth of the α -FeSi₂ (Ref. 29) and β -FeSi₂ (Refs. 17, 18, 20–22, 28, and 30–35) have been reported. The Fe silicide growth

on Si(111) surface is quite a complicated system because the formations and morphologies of these phases strongly depend on the various growth conditions. Many authors have shown several epitaxial phases on Si(111) surfaces by various growth techniques: solid phase epitaxy (SPE)—i.e., a substrate is held at room temperature (RT) during Fe deposition and subsequently annealed^{13,14,18–38} reactive deposition epitaxy (RDE)—i.e., a substrate is held at high temperature during Fe deposition^{23,28,39}—and codeposition of Si and Fe,^{15–17,40} and other methods. However, almost all previous reports showed results focused on only partial silicide formation; differences and complexities in growth conditions make it difficult to compare the formation of the different silicide phases from the results. To understand the overall view regarding the formations and changes of several Fe silicide phases on Si(111) surfaces and their growth mechanisms, it is necessary to investigate silicide formations using a simple and typical growth method.

In this paper, we show all the above Fe silicide phases with different surface structures and morphologies formed on Si(111)7×7 surfaces using SPE growth. The SPE is a simple growth method because the reaction is essentially only a function of the Fe coverage and the subsequent annealing temperature. Therefore, each result of silicide formation in the SPE growth can provide a systematic explanation of the complicated silicide growth processes in a Si(111)-Fe system. In our study, low-energy electron diffraction (LEED) and scanning tunneling microscopy (STM) were used to characterize surface periodic structures and morphologies of silicide phases. Reflection high-energy electron diffraction (RHEED) was also used for three-dimensional (3D) structure analysis. From these measurements, we determined the schematic phase diagram in detail with high reliability, which is an important result for future detailed structural analysis. Moreover, we found several characteristic structures additionally: the δ -7×7 structure, facets in the bcc-Fe(111)1×1 phase, tilts of the $\sqrt{3}\times\sqrt{3}$ phase, a new superstructure of the β -FeSi₂ surface, and others. Below we describe detailed morphological and structural information

for each phase, and discuss the growth mechanisms of silicide structures on Si(111) surfaces.

II. EXPERIMENT

Experiments were carried out in an ultrahigh vacuum (UHV) system⁸ equipped with LEED and STM. A base pressure of the chamber was less than 1×10^{-8} Pa. A substrate was cut from an Sb-doped, *n*-type, mirror-polished Si(111) wafer with a resistivity of $0.02 \Omega \text{ cm}$. The Si(111) sample was introduced into the chamber and was degassed by direct current heating. After repeated flashings at approximately 1250°C under $2\text{--}3 \times 10^{-8}$ Pa, a clean Si(111) 7×7 reconstructed surface was obtained. The Si(111) 7×7 structure was confirmed by LEED and STM. Silicide layers were grown by the SPE method: iron was deposited onto a Si(111) 7×7 surface which was maintained at RT ($<50^\circ \text{C}$) and the sample was subsequently annealed. Once Fe silicide layers were formed on the Si(111) surface, the surface order did not recover completely by means of the flashing process. Thus, the sample was replaced by a new one for every cycle of Fe deposition. Iron was evaporated from an alumina crucible with Fe solid source (99.999%) under $5\text{--}6 \times 10^{-8}$ Pa. The deposition rate (typically, $0.3\text{--}0.9 \text{ \AA}/\text{min}$) and the Fe coverage θ_{Fe} were monitored by a quartz crystal oscillator. We define a unity monolayer (ML) as the surface atomic density of an unreconstructed Si(111) plane: 7.83×10^{14} atoms/cm². Subsequent annealing temperatures T_a ranged from 300 to 800°C in steps of 100°C and maintained for 10 min. The temperature was measured by an optical pyrometer. After each annealing, the sample was cooled to RT and characterized by LEED and STM. In STM measurements, we observed current images using electrochemically etched W tips. The tunneling current was $0.3\text{--}0.5$ nA. We also observed RHEED transmission patterns in another UHV system,⁷ to analyze structures and epitaxial relationships of 3D islands. To determine the phase diagram, these characterizations were carried out at 23 different Fe coverages (0.2, 0.7, 0.9, 1.0, 1.3, 1.7, 2.0, 2.6, 4.0, 4.6, 5.3, 6.6, 7.3, 7.9, 12, 16, 24, 28, 32, 37, 40, 48, and 56 ML).

III. RESULTS AND DISCUSSION

A. Schematic phase diagram

Figure 1 shows the schematic phase diagram of Fe silicides grown by SPE on a Si(111) surface determined in detail by LEED and STM measurements. In the SPE growth, $\delta\text{-}7 \times 7$, 1×1 , $\text{bcc-Fe}(111) 1 \times 1$, 2×2 , $c(8 \times 4)$, $3\text{D-}2 \times 2$ ($\alpha\text{-FeSi}_2$), $\sqrt{3} \times \sqrt{3}\text{-R}30^\circ$, $\beta\text{-FeSi}_2$, and fine polycrystalline phases are formed on the Si(111) surface as a function of Fe coverage and subsequent annealing temperature. We confirmed that the phase diagram did not change much with an extra 10–30 min annealing and that the deposition rate and other factors did not affect the diagram significantly, at least within the conditions described in Sec. II. Therefore, we consider that this schematic phase diagram is highly reliable. In the following subsections, Secs. III B–III G, we reveal the detailed morphology and the change in each phase. In Sec.

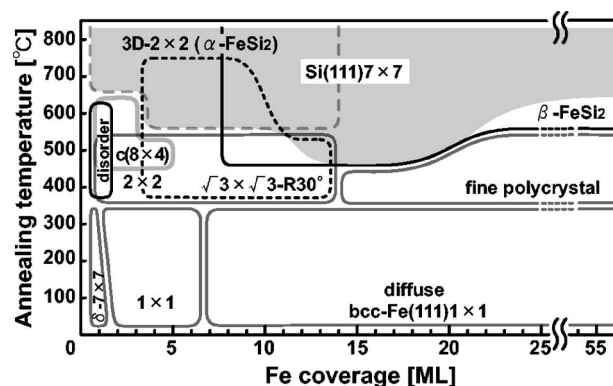


FIG. 1. The schematic phase diagram of a SPE-grown Si(111)-Fe surface observed at RT. The Si(111) 7×7 surface deposited with Fe at RT is subsequently annealed for 10 min. The gray zone indicates the reappeared Si(111) 7×7 structure.

III H, we discuss the growth mechanisms based on the schematic phase diagram and the morphological information.

B. $\delta\text{-}7 \times 7$ and 1×1 phases

At the initial destruction process of the 7×7 structure during Fe deposition at RT, we observed the formation of the $\delta\text{-}7 \times 7$ structure.⁴¹ The Si(111) 7×7 LEED pattern gradually blurs and changes to a $\delta\text{-}7 \times 7$ pattern [Fig. 2(a)] retaining the part of the weak 7×7 spots with higher background intensity. In another system of atomic hydrogen exposed to a Si(111) 7×7 surface,⁴² the $\delta\text{-}7 \times 7$ LEED pattern has been reported. The STM work has suggested that the adsorbed hydrogen atoms break the Si adatom back bonds, resulting in the removal of the adatoms.⁴³ Therefore, the appearance of the $\delta\text{-}7 \times 7$ structure indicates that 7×7 adatoms move from their original positions by deposited Fe atoms with the first and second layer remaining. In the STM image [Fig. 2(b)], the 7×7 adatom arrangements are not observed but the surface is covered by clusters with about 7×7 half-unit size. In this stage, we found that the silicide clusters are grown by the reactions mostly between 7×7 adatoms and deposited Fe atoms.

At $\theta_{\text{Fe}} \sim 1.7$ ML, the 7×7 LEED spots completely disappear but the 1×1 fundamental spots remain. This implies

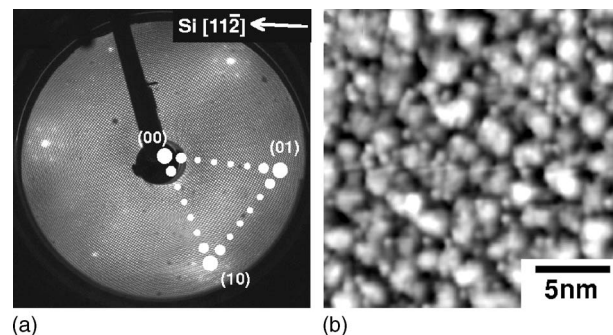


FIG. 2. (a) A LEED pattern and (b) an STM image obtained at $\theta_{\text{Fe}}=0.9$ ML and $T_a=\text{RT}$ [the observation conditions were (a) primary energy $E_p=40$ eV and (b) sample bias voltage $V_s=+1.0$ V].

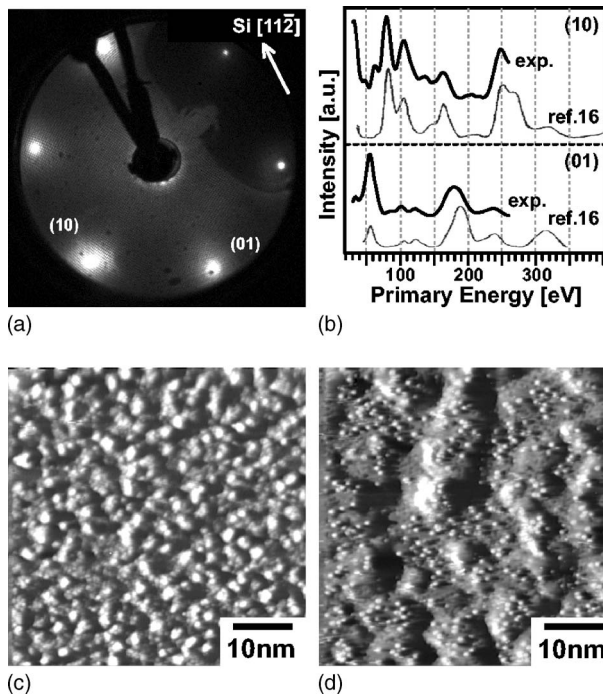


FIG. 3. (a) A LEED pattern, (b) LEED $I(E_p)$ curves, and (d) an STM image obtained at $\theta_{Fe}=4.6$ ML and $T_a=300$ °C and (c) an STM image at $\theta_{Fe}=4.6$ ML and $T_a=RT$ [(a) $E_p=35$ eV, (c) $V_s=+0.7$ V, and (d) $V_s=+1.0$ V]. The black and gray curves in (b) show experimental LEED $I(E_p)$ curves for (10) and (01) spots in this work and Ref. 16 [B2 FeSi(111)1×1 film], respectively.

that almost all 7×7 reconstructed Si atoms—i.e., the first and second-layer atoms—are reacted. The 1×1 LEED pattern is retained up to $T_a=300$ °C, indicating the same lattice constant as the Si(111) plane [Fig. 3(a)]. From intensity versus primary energy $I(E_p)$ curves obtained from (10) and (01) spots for the 1×1 pattern at $T_a=300$ °C [Fig. 3(b)], we confirmed that peak positions and intensity distributions were similar to those of epitaxially stabilized FeSi(111)1×1 films with a CsCl (B2) structure.^{13,14,16,17} Therefore, we can identify the 1×1 phase for $T_a=300$ °C as a B2-FeSi(111)1×1 structure.

The STM image at $T_a=RT$ [Fig. 3(c)] shows a great number of clusters with a few nanometers size on the surface. We assign the small clusters to Fe clusters or iron-silicide clusters with high Fe concentration, since an Fe film starts to grow in the next stage of Fe deposition. We suggest that the small clusters play a role in the nucleation centers for Fe growth; an inhomogeneously shaped pure bcc-Fe(111) film grows as shown in the following subsection, Sec. III C. The surface morphology after 300 °C annealing is considerably different from that of the as-deposited sample. The STM image after 300 °C annealing [Fig. 3(d)] shows very small protrusions in sizes of less than 1 nm randomly distributed over the rough surface. We assign the very small protrusion to a Si adatom, because silicon has a tendency to segregate in silicide by annealing.²⁰ Actually, the existence of Si adatoms at this stage²⁶ and the next-annealing stage (2×2 phase) (Refs. 19, 20, and 25) has been pointed out in several studies.

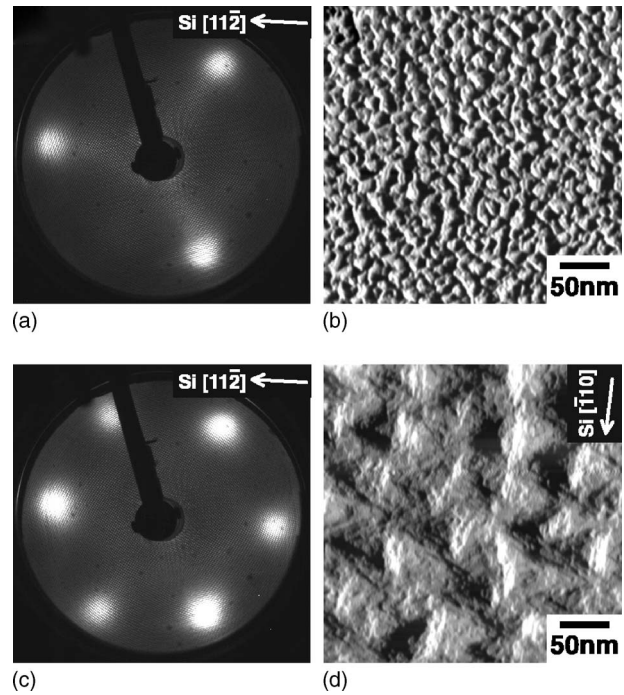


FIG. 4. LEED patterns and STM images obtained at (a), (b) $\theta_{Fe}=37$ ML and $T_a=RT$ and (c), (d) $\theta_{Fe}=37$ ML and $T_a=300$ °C [(a), (c) $E_p=35$ eV, (b) $V_s=+1.0$ V, and (d) $V_s=+1.5$ V].

C. bcc-Fe(111)1×1 phase

At $\theta_{Fe}\geq 7$ ML, an Fe(111)1×1 pattern with surface unit length of 0.406 nm appears instead of the Si(111)1×1 or FeSi(111)1×1 with surface unit length of 0.384 nm. The LEED pattern [Fig. 4(a)] shows broad spots and the characteristic trigonal symmetry of the 1×1 pattern with the same lattice constant as the bcc-Fe(111) plane. The domain size estimated from the broadening of the 1×1 LEED spots is very small ($\sim 1-2$ nm). From RHEED transmission patterns obtained from different electron-incident directions, we confirmed the growth of the bcc-Fe(111) structure and azimuth orientation: Fe(111)∥Si(111) with Fe $[\bar{1}\bar{1}\bar{2}]$ ∥Si $[\bar{1}\bar{1}\bar{2}]$ —i.e., B-type stacking. The same azimuth orientation of the bcc-Fe(111) structure grown on Si(111) surface has been proposed by x-ray diffraction (XRD) and transmission electron diffraction (TED) work³³ and coaxial impact-collision ion scattering spectroscopy work.³⁴ The STM image at $T_a=RT$ [Fig. 4(b)] reveals a 3D-grown inhomogeneous-shaped bcc-Fe(111) film; the surface is not smooth and is covered with randomly shaped small grains (5–20 nm).

After 300 °C annealing, the STM image [Fig. 4(d)] reveals somewhat large triangle like bumps. The bcc-Fe(111) LEED pattern is retained up to $T_a=300$ °C [Fig. 4(c)], and the domain size ($\sim 1-2$ nm) did not increase much by 300 °C annealing. The RHEED transmission patterns also showed the similar patterns as that of the as-grown sample, but each spot became streaky which implies the formation of thinner bcc-Fe(111) film—that is, lower height of the bumps—in comparison with the as-deposited sample. The streaks in the RHEED patterns appear as the hexagonal-like symmetric spots in the LEED pattern [Fig. 4(c)].

Furthermore, in LEED patterns at $T_a = \text{RT}$ and 300°C , we observed spots originated from facets, though we hardly identify them in STM images. From the analysis in $E_p = 20\text{--}240\text{ eV}$, we found several facets: the $T_a = \text{RT}$ samples showed tilt angles of $\approx 15^\circ$ and $\approx 17^\circ$ in three Si $\langle 11\bar{2} \rangle$ azimuth directions, $\approx 9^\circ$ and $\approx 14^\circ$ in Si $\langle \bar{1}\bar{1}2 \rangle$ and $\approx 18^\circ$ in Si $\langle 13\bar{4} \rangle$ and Si $\langle 31\bar{4} \rangle$. The $T_a = 300^\circ\text{C}$ samples showed tilt angles of $\approx 12^\circ$ and $\approx 17^\circ$ in three Si $\langle 11\bar{2} \rangle$ azimuth directions, $\approx 12^\circ$, $\approx 13^\circ$, and $\approx 14^\circ$ in Si $\langle \bar{1}\bar{1}2 \rangle$, and $\approx 17^\circ$ in Si $\langle 13\bar{4} \rangle$ and Si $\langle 31\bar{4} \rangle$. These results indicate anisotropic growth of the bcc (111) with some facets.

D. 2×2 and $c(8 \times 4)$ phases

At $T_a \geq 400^\circ\text{C}$, several silicide surface structures are clearly observed depending on θ_{Fe} and T_a . At $\theta_{Fe} \leq 3\text{ ML}$ and $T_a \geq 400^\circ\text{C}$, 2×2 , $c(8 \times 4)$, and $3\text{D-}2 \times 2$ phases are grown on the substrate without coexistence with the $\sqrt{3} \times \sqrt{3}\text{-R}30^\circ$ phase. At lower Fe coverage of $\theta_{Fe} \leq 1.5\text{ ML}$, atomically flat domains with 2×2 periodic structure are formed in a disordered substrate. We observed the ring structures²⁴ in the disordered substrate at $T_a = 300\text{--}400^\circ\text{C}$.

At slightly higher Fe coverage than $\sim 1.5\text{ ML}$, the surface is fully covered with the 2×2 or $c(8 \times 4)$ films depending on T_a . We found that the suitable range of Fe coverage for the single phase formation of the 2×2 or $c(8 \times 4)$ films is very narrow ($\theta_{Fe} \sim 1.5\text{--}3\text{ ML}$) due to the coexistence with the $\sqrt{3} \times \sqrt{3}\text{-R}30^\circ$ phase at $\theta_{Fe} \geq 3\text{ ML}$ (Fig. 1). Figures 5(a) and 5(b) show a sharp 2×2 LEED pattern and an STM image, respectively, at $\theta_{Fe} = 1.7\text{ ML}$ and $T_a = 400^\circ\text{C}$. The STM image shows that the 2×2 structure covers the surface and that randomly shaped small islands with 2×2 structures form on the 2×2 substrate. An atomic-resolved image of the 2×2 arrangements on the surface is shown in the inset of Fig. 5(b). With increasing T_a , the 2×2 area starts to change to the $c(8 \times 4)$ phase and the island shape changes to a hexagonal shape⁸ and then to a triangular shape. After annealing at 600°C , the 2×2 phase completely transformed to the $c(8 \times 4)$ phase as shown in Figs. 5(c) and 5(d). The LEED pattern [Fig. 5(c)] indicates a $c(8 \times 4)$ pattern with three equivalent domains rotated by 120° . The STM image [Fig. 5(d)] reveals the $c(8 \times 4)$ terraces and the $c(8 \times 4)$ triangle-shaped islands with Si $\langle \bar{1}10 \rangle$ direction edges. On the surface, well-ordered $c(8 \times 4)$ arrangements are seen as shown in the inset of Fig. 5(d). The $c(8 \times 4)$ surface consists of bright and dark protrusions in the 2×2 arrangements. We found that the $c(8 \times 4)$ phase did not appear at higher coverage of $\theta_{Fe} \geq 5\text{ ML}$: the thicker 2×2 films are not able to transform to the $c(8 \times 4)$ phase. The enhancement of the $c(8 \times 4)$ phase at the higher T_a and smaller θ_{Fe} suggests a diluted Fe density of the $c(8 \times 4)$ phase.

For the 2×2 phase, two structural models have been proposed. One is $\gamma\text{-FeSi}_2$ with CaF_2 structure suggested by RHEED and AES work¹⁸ and by STM works^{14,19,20} and the other is FeSi_{1+x} ($0 \leq x \leq 1$) with a defect CsCl structure derived from randomly distributed Fe vacancies suggested by XPS, transmission electron diffraction (TEM), and TED work¹⁵ and by STM works.^{23,24} Moreover, we should note

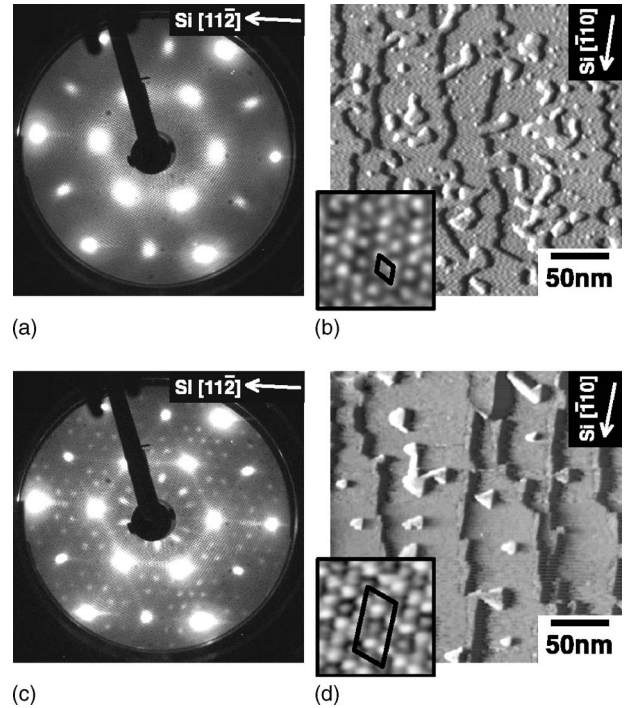


FIG. 5. LEED patterns and STM images of (a), (b) 2×2 and (c), (d) $c(8 \times 4)$ phases, obtained at $\theta_{Fe} = 1.7\text{ ML}$, and (a), (b) $T_a = 400^\circ\text{C}$ and (c), (d) $T_a = 600^\circ\text{C}$ [(a), (c) $E_p = 35\text{ eV}$ and (b), (d) $V_s = +1.0\text{ V}$]. Atomically resolved (b) 2×2 surface unit and (d) $c(8 \times 4)$ surface unit are shown in the insets.

that some authors have pointed out a transformation from CsCl structure to CaF_2 structure as temperature increases in the 2×2 phases for SPE growth.^{21,22} In also our previous reports, the CsCl-based structure (CsCl and CaF_2 structure) for the SPE-grown ultrathin 2×2 films has been confirmed by a stereo atomscope using photoelectron angular distribution patterns³⁸ and by a 3D-RHEED Patterson function calculation.⁴⁴ For the $c(8 \times 4)$ has phase, it has been suggested that the structure model with 2×2 Si adatoms on the CsCl structure has ordered Fe vacancies.²⁶

E. $3\text{D-}2 \times 2$ ($\alpha\text{-FeSi}_2$) phase

At higher annealing temperature at $T_a = 600$ or 700°C and $\theta_{Fe} \leq 14\text{ ML}$, the $2\text{D-}2 \times 2$ or $c(8 \times 4)$ phases disappear, and elongated 3D islands with 2×2 surfaces are formed, in addition to the reappeared Si(111) 7×7 structure. Figures 6(a) and 6(b) show a 2×2 LEED pattern superimposed on the 7×7 pattern and an STM image, respectively, at $\theta_{Fe} = 1.3\text{ ML}$ and $T_a = 700^\circ\text{C}$. Figure 6(b) shows a typical STM image at a region of 3D-grown islands, indicating that segregated and elongated islands of $\sim 100\text{ nm}$ in length are grown toward three Si $\langle \bar{1}10 \rangle$ directions. On the tops of the 3D islands, 2×2 [not $c(8 \times 4)$] arrangements are seen with several (2×2) -periodic protrusions in width [in the inset of Fig. 6(b)]. The $3\text{D-}2 \times 2$ islands as shown in Fig. 6(b) occupied a part of the surface, and the rest were the Si(111) 7×7 region. The $3\text{D-}2 \times 2$ phase does not coexist with the flat 2×2 or $c(8 \times 4)$ phases, while it does with 7×7 , $\sqrt{3} \times \sqrt{3}\text{-R}30^\circ$

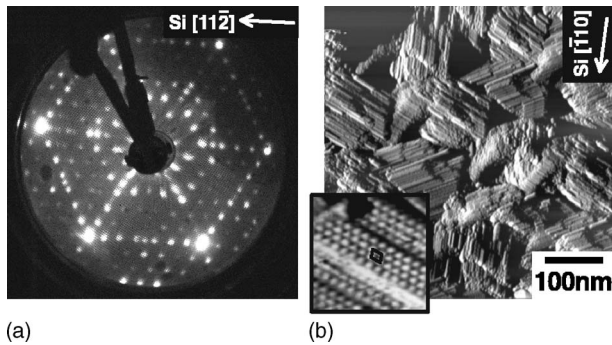


FIG. 6. (a) A LEED pattern and (b) an STM image of the 3D- 2×2 phase obtained at $\theta_{Fe}=1.3$ ML and $T_a=700$ °C [(a) $E_p=35$ eV and (b) $V_s=+1.0$ V].

$R30^\circ$, and β -FeSi₂ phases (Fig. 1). In addition, the 3D- 2×2 phase is formed at slightly higher T_a than the formations of the flat 2×2 and $c(8 \times 4)$ phases. These results strongly suggest that the atoms consisting of the flat 2×2 and $c(8 \times 4)$ phases aggregate to the 3D- 2×2 islands.

The previous STM work suggested the CsCl structure for the SPE-grown 3D- 2×2 islands.²⁴ The previous RHEED work presented a reciprocal lattice of the RDE-grown 3D- 2×2 phase.³⁹ We observed almost the same RHEED transmission patterns as reported in Ref. 39. The reciprocal lattice corresponds to the tetragonal α -FeSi₂ structure studied with XRD: α -FeSi₂ (112)||Si(111) with α -FeSi₂ [$1\bar{1}0$]|Si($\bar{1}10$), Si[$0\bar{1}1$], and Si[$10\bar{1}$].²⁹ Therefore, we can assign the 3D- 2×2 phase obtained here to the α -FeSi₂ structure. Since the α -FeSi₂ (112) plane has onefold symmetry, this structure is able to explain the elongated character of the 3D- 2×2 islands from the lattice mismatch with the Si(111) substrate: -1.0% for α -FeSi₂ [$1\bar{1}0$] and -4.0% for α -FeSi₂ [$\bar{1}\bar{1}1$]. We emphasize that the α -FeSi₂ phase in bulk is stable only at high temperature (937–1220 °C).¹¹ Thus, we consider that the interface with Si(111) substrate stabilizes the high-temperature bulk phase α -FeSi₂, which determines the shape of the elongated 3D- 2×2 islands of the α -FeSi₂ structure at RT. The surface of the 3D islands should be reconstructed with 2×2 arranged Si adatoms.

F. $\sqrt{3} \times \sqrt{3}$ -R30° phase

At $\theta_{Fe} \sim 3$ –14 ML and $T_a=400$ –700 °C, the $\sqrt{3} \times \sqrt{3}$ -R30° phase is grown, which does not appear alone and partially coexists with other silicide phases [2×2 , $c(8 \times 4)$, 3D- 2×2 (α -FeSi₂), and β -FeSi₂] in some conditions. A LEED pattern and an STM image at $\theta_{Fe}=4.0$ ML and $T_a=500$ °C are shown in Figs. 7(a) and 7(b), respectively. In this condition, the 2×2 , $c(8 \times 4)$, and $\sqrt{3} \times \sqrt{3}$ phases coexist (Fig. 1), though the $c(8 \times 4)$ phase is not dominant as shown in Fig. 7(a). The STM image [Fig. 7(b)] reveals that the surface is almost covered with the 2×2 arrangements and that randomly distributed roundlike-shaped $\sqrt{3} \times \sqrt{3}$ domains (some are indicated by arrows) in size of a few tens nm are grown. We notice that almost all $\sqrt{3} \times \sqrt{3}$ domains are ditched around. The ditches were also observed on higher- T_a

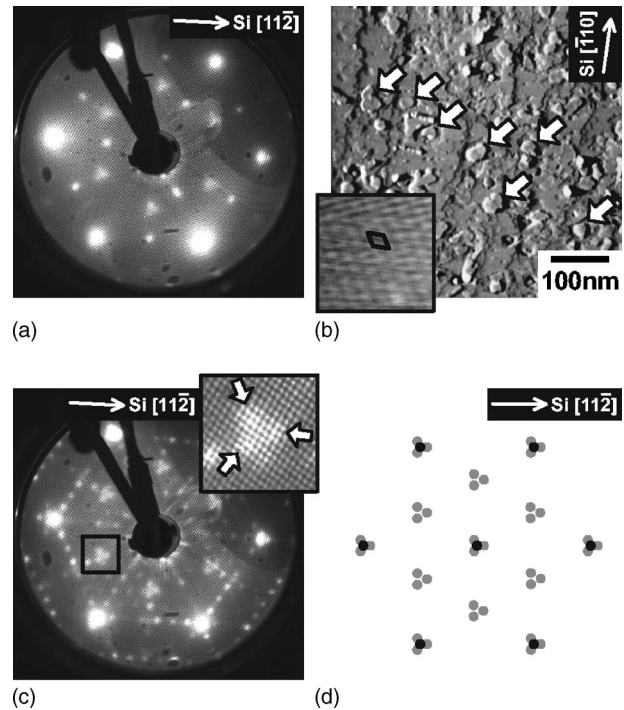


FIG. 7. LEED patterns of the (a) $\sqrt{3} \times \sqrt{3}$ -R30° phase superposed on 2×2 and extremely weak $c(8 \times 4)$ phases and (c) $\sqrt{3} \times \sqrt{3}$ -R30° phase superposed on 2×2 and 7×7 phases and (b) an STM image of mixture surface of $\sqrt{3} \times \sqrt{3}$ -R30° domains (some of them are indicated by arrows) and 2×2 domains (the others), obtained at $\theta_{Fe}=4.0$ ML, and (a), (b) $T_a=500$ °C and (c) $T_a=600$ °C [(a), (c) $E_p=45$ eV and (b) $V_s=+1.0$ V]. (d) A schematic illustration of the split $\sqrt{3} \times \sqrt{3}$ -R30° LEED pattern. An atomically resolved $\sqrt{3} \times \sqrt{3}$ -R30° domain and a magnified $\sqrt{3} \times \sqrt{3}$ spot are shown in the insets in (b) and (c), respectively.

samples where the 7×7 area surrounds the $\sqrt{3} \times \sqrt{3}$ domains. On these atomically flat domains, the $\sqrt{3} \times \sqrt{3}$ periodic structure is observed with weak corrugations as shown in the inset of Fig. 7(b). At higher T_a such as 600 or 700 °C, we found that the $\sqrt{3} \times \sqrt{3}$ domain size somewhat enlarges but the $\sqrt{3} \times \sqrt{3}$ domain does not grow to a 3D island, while 3D- 2×2 islands are formed. Furthermore, the $\sqrt{3} \times \sqrt{3}$ LEED spot intensity was maximum at $\theta_{Fe} \sim 5$ ML, and the intensity decreased and the spots became broader with increasing θ_{Fe} , indicating restricted $\sqrt{3} \times \sqrt{3}$ domain size.

We found that the $\sqrt{3} \times \sqrt{3}$ related spots split in the LEED pattern into three directions along Si[$11\bar{2}$], Si[$\bar{2}11$], and Si[$1\bar{2}1$] and that the split becomes clearer at higher annealing temperature. Figure 7(c) shows a LEED pattern for superimposed 7×7 , 2×2 , and $\sqrt{3} \times \sqrt{3}$ phases at $\theta_{Fe}=4.0$ ML and $T_a=600$ °C. A schematic illustration of the split $\sqrt{3} \times \sqrt{3}$ pattern is shown in Fig. 7(d). Since no superstructures with much longer periodicity were observed in STM and no reverse-direction spots of the split ones for $E_p=10$ –150 eV were observed in LEED, it is hard to explain the split from the long-periodicity modulated superstructure or the deformation of the $\sqrt{3} \times \sqrt{3}$ domains. Consequently, we suggest that the split is derived from tilts of the $\sqrt{3} \times \sqrt{3}$ plane toward three Si($11\bar{2}$) directions. From analysis of

the LEED pattern, we estimated the tilt angle to be approximately 0.8° .

The formation of the $\sqrt{3} \times \sqrt{3}$ -R30° structure has been reported by other LEED,^{22,27} RHEED,^{18,28} STM,²⁰ and XRD²⁸ works. The diffraction works proposed the epitaxy of B20 ϵ -FeSi(111)[110]||Si(111)[112].^{18,22,28} In this case the bulk cubic ϵ -FeSi structure has an isotropic lattice mismatch with the Si(111) substrate of -4.3% . We point out that the strain resulting in the isotropic expansion of the ϵ -FeSi(111) plane can explain the restricted domain size, the roundlike shape, the ditches, and the tilted domain, qualitatively.

G. β -FeSi₂ and fine polycrystalline phases

At $\theta_{Fe} \geq 8$ ML and $T_a \geq 500$ or 600 °C, a characteristic β -FeSi₂ LEED pattern is observed [Fig. 8(a)]. In SPE growth, this LEED pattern has been attributed to the epitaxial orthorhombic β -FeSi₂ phase.³⁰ The β -FeSi₂(101) and (110) units (0.78 nm \times 1.26 nm) match well with the Si(111) lattice [dashed lines in Fig. 8(e)] and have been confirmed by TEM analysis for the SPE-grown β -FeSi₂ phase.³¹ The LEED pattern in Fig. 8(a) shows superimposed equivalent three domains rotated by 120° of rectangle units (an estimated unit size is 0.78 ± 0.01 nm \times 0.62 ± 0.01 nm) corresponding to half of the β -FeSi₂(101) or (110) plane [gray zone in Fig. 8(e)], which have been reported previously.³⁷ We emphasize that the LEED result indicates that the primitive unit is half the size of the β -FeSi₂(101) or (110) plane at least in a few layers of the epitaxial β -FeSi₂ films. A complex orthorhombic β -FeSi₂ bulk structure can be treated as distorted $2 \times \sqrt{2} \times \sqrt{2}$ fluorite (γ -FeSi₂) structure rotated by approximately 45° in β -FeSi₂(100) plane.⁴⁵ The half-size unit indicates that the β -FeSi₂ surface layers consist of a differently distorted structure from the β -FeSi₂ bulk: the half period of the a axis.

We observed squarelike-shaped 3D β -FeSi₂ islands with flat terraces in various sizes and heights as shown in Fig. 8(b). The edges of the islands tend to be along Si $[\bar{1}10]$ and Si $[11\bar{2}]$ directions, and in the other scanning area we confirmed squarelike islands rotated by $\pm 120^\circ$. The morphology did not depend on θ_{Fe} , though with increasing T_a the islands grow higher and 7×7 substrate structure reappears.

In atomic-resolved STM images on the atomically flat terrace [Figs. 8(c) and 8(d)], several complex surface structures are observed. On most of the β -FeSi₂ surfaces, it was difficult to find a clear atomically periodic structure, but many characteristic stripes along Si $[\bar{1}10]$ directions were seen. The stripes have been assigned to an intrinsic stacking fault due to relaxations of the large strain along Si $\langle 11\bar{2} \rangle$ directions (-5.3% or -5.5%) compared with Si $\langle \bar{1}10 \rangle$ directions ($+1.4\%$ or $+2.0\%$).³² This domain restriction toward Si $\langle 11\bar{2} \rangle$ directions reflects the streaks in these direction in the LEED pattern [Fig. 8(a)]. We observed that the stripes with the same direction along the island edge (Si $[\bar{1}10]$, Si $[0\bar{1}1]$, or Si $[10\bar{1}]$) are formed across the islands at least in the region of several hundreds nm.

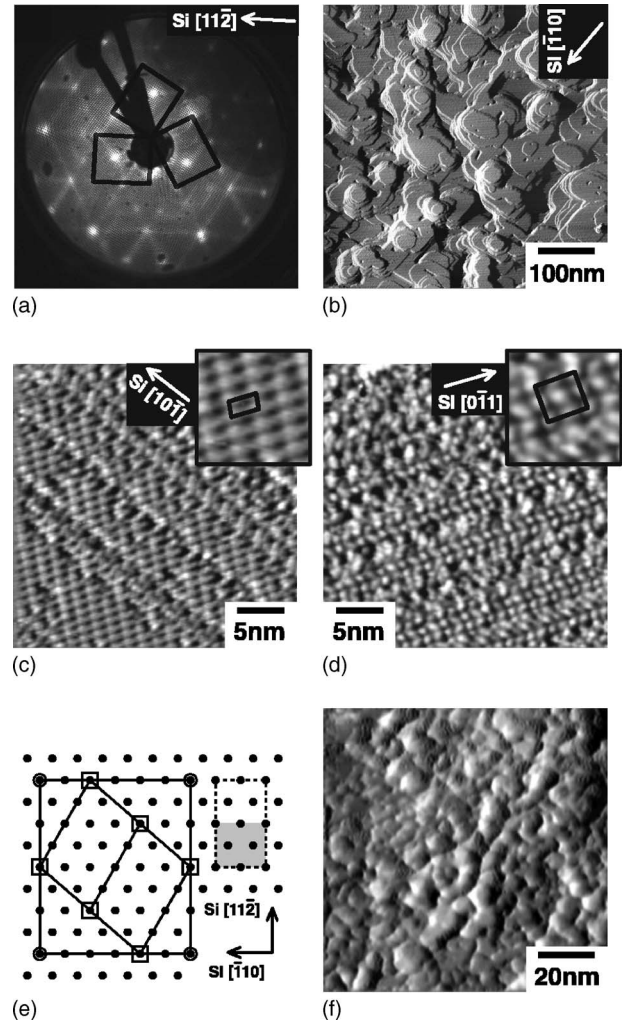


FIG. 8. (a) A LEED pattern and (b), (c), (d) STM images of the β -FeSi₂ phase and (f) an STM image of fine polycrystalline phase, obtained at (a) $\theta_{Fe}=28$ ML and $T_a=600$ °C, (b) $\theta_{Fe}=40$ ML and $T_a=600$ °C, (c) $\theta_{Fe}=24$ ML and $T_a=600$ °C, (d) $\theta_{Fe}=28$ ML and $T_a=600$ °C, and (f) $\theta_{Fe}=37$ ML and $T_a=400$ °C [(a) $E_p=35$ eV, (b), (d) $V_s=+1.0$ V, and (c), (f) $V_s=-1.0$ V]. Magnified images of (c) the parallelogram unit and (d) the rectangular unit are shown in the each inset. (e) Schematic illustration of epitaxial relationships of the β -FeSi₂(101) or (110) plane (dashed lines) on the Si(111) 1×1 primitive units (solid circles). The observed β -FeSi₂ unit in LEED is displayed by the gray zone. The observed parallelogram and rectangular units are displayed by open squares and open circles, respectively.

Between the stripes, two surface periodic structures were observed. One is a previously reported^{32,40} parallelogram unit [Fig. 8(c)] (1.53 ± 0.08 nm \times 1.01 ± 0.05 nm) with approximately 84° , lying at an angle of approximately 40° between the short side of the unit and Si $[\bar{1}10]$ direction. We found another surface structure, rectangle unit [Fig. 8(d)] (2.40 ± 0.12 nm \times 2.52 ± 0.12 nm). The arrangements of the parallelogram and rectangle units are shown as enclosed units marked by open squares and open circles in Fig. 8(e), respectively. We found that these two surface structures do not depend on θ_{Fe} and T_a , indicating that these structures are

more stable structures in the SPE-grown β -FeSi₂. We emphasize that these two surface units can be represented by superstructures based on the half unit of the β -FeSi₂ (101) or (110) plane [the gray zone in Fig. 8(e)]. The rectangle unit corresponds to 3×4 reconstruction, and the parallelogram unit corresponds to $\begin{pmatrix} 1 & 2 \\ -1 & 1 \end{pmatrix}$ reconstruction, on the basis of the half unit. The STM images in Figs. 8(c) and 8(d) would display Si adatom protrusions of the metastable reconstructed structures arising from different stacking faces.

At $\theta_{Fe} \geq 14$ ML and $T_a = 400$ – 500 °C, LEED spots disappeared (fine polycrystalline phase). The disappearance of the diffraction spots has been reported by others.^{15,18,35,36} Figure 8(f) shows a typical STM image, indicating a rough morphology (~ 10 nm grains) with no periodic structure in the atomic scale. RHEED patterns showed Debye rings, indicating the formation of fine polycrystals.⁷ In the similar phase (disordered phase) in the codeposition system, the presence of heavily twinned ϵ -FeSi has been reported using TEM analysis.¹⁵

H. Growth mechanisms

The detailed morphologies for each Fe silicide phases were revealed in previous Secs. III B–III G. We discuss the growth mechanisms from the morphologies and the schematic phase diagram (Fig. 1), which should be determined by the kinetic and thermodynamic processes of the Fe-Si binary system basically. We notice three dominant annealing stages of the Fe silicide growth for all θ_{Fe} .

In stage I ($T_a \leq 300$ °C), the epitaxially stabilized B2 FeSi and Fe films survive under the annealing; however, their quality and morphologies changed by the annealing. At lower θ_{Fe} , the annealing leads to the disappearance of the small Fe or iron-silicide clusters and the segregation of Si adatoms on a well-ordered B2 FeSi(111) 1×1 phase grown over wide areas on the substrate. At higher θ_{Fe} , the annealing leads to the disappearance of small Fe(111) grains and the aggregation of Fe atoms, forming a thinner Fe(111) 1×1 rough surface. Obviously, this stage corresponds to the interdiffusion within the films.

In stage II (400 °C $\leq T_a \leq 500$ – 600 °C), the mixing of atoms between the films and Si substrate occurs additionally and new metastable films form in the nonequilibrium condition. At lower θ_{Fe} (≤ 3 ML), the Si segregation and the Fe diffusion lead to well-ordered films with the 2×2 and $c(8 \times 4)$ surface structures, which have the B2 FeSi-based structures (CsCl, defect CsCl, and CaF₂). The film thickness of these phases are several layers since they are stable for $\theta_{Fe} \sim 1.5$ – 3 ML (Fig. 1). According to density-functional calculations,⁴⁶ the B2 FeSi bulk structure (calculated lattice constant 0.277 nm) is a little bit unstable than B20 ϵ -FeSi bulk structure. We emphasize that the excellent lattice matching of the B2 FeSi-based structures with the Si(111) substrate can form 2×2 and $c(8 \times 4)$ phases with a restricted height of several layers. At middle θ_{Fe} (3–14 ML), the $\sqrt{3} \times \sqrt{3}$ domains appear in the 2×2 or $c(8 \times 4)$ films. We proposed the expanded ϵ -FeSi(111) structure for the $\sqrt{3} \times \sqrt{3}$

domain in Sec. III F. The thermal stability of the $\sqrt{3} \times \sqrt{3}$ domains even at the next-annealing stage also suggests the formation of ϵ -FeSi, since ϵ -FeSi is stable in a wide range at ≤ 1410 °C (Ref. 11) and one of the most stable bulk phases. The disturbance of the $\sqrt{3} \times \sqrt{3}$ domain formation by extra Fe atoms at $\theta_{Fe} \geq 5$ ML suggests that some thick ϵ -FeSi(111) regions cannot be pinned by the substrate and start to grow as 3D islands with random orientations. With increasing θ_{Fe} other stoichiometry silicides would also grow, reflecting the fluctuation of the initial iron distribution. The fine polycrystalline phase should include such small 3D islands with some stoichiometry between Fe and FeSi₂, which could form under the nonequilibrium condition.

In stage III ($T_a \geq 500$ – 700 °C), the massive interdiffusion between the silicide films [2×2 , $c(8 \times 4)$, or fine polycrystalline phases] and substrate destroys their structures, leading to the stable phases near the equilibrium condition: the $\sqrt{3} \times \sqrt{3}$ domains, the 3D α -FeSi₂ islands, the 3D β -FeSi₂ islands, and the Si(111) 7×7 substrate. We note that bulk phases with excellent lattice matching axis with the substrate can grow as 3D islands (α -FeSi₂: -1.0% and β -FeSi₂: $+1.4\%$ or $+2.0\%$) while the bulk phase with poor lattice matching forms film-shaped small domains (ϵ -FeSi: -4.3%). The α -FeSi₂ forms at lower θ_{Fe} , and the β -FeSi₂ is formed at higher θ_{Fe} . Obviously, this result indicates a larger formation energy gain of the α -FeSi₂ (high-temperature phase in bulk) islands pinned by the Si(111) substrate directly. The change from α -FeSi₂ to β -FeSi₂ with increasing θ_{Fe} would be caused by the instability of the bulklike α -FeSi₂ islands, of which the bulk phase is unstable at RT, with larger volume at higher θ_{Fe} .

IV. SUMMARY

We determined the reliable and complete schematic phase diagram of Fe silicides grown by SPE on a Si(111) surface by LEED and STM measurements depending on Fe coverage and subsequent annealing temperature. This detailed map is useful for future detailed structure analysis and others. For all phases, we revealed the morphologies and their changes. In particular, we newly found that the formation of the δ - 7×7 structure, the several facets for 3D-grown inhomogeneous-shaped bcc-Fe(111) films, the tilts of the roundlike small $\sqrt{3} \times \sqrt{3}$ - $R30^\circ$ domains, and the rectangle surface units on the squarelike β -FeSi₂ wide islands. From such a detailed morphological information and the schematic phase diagram, we discussed the growth mechanisms. The overall view of the formations of SPE-grown Fe silicide phases, including a detailed morphology of each phase, provides us with some hints to understand the growth mechanism of ultrathin Fe silicide phases on Si substrates.

ACKNOWLEDGMENT

We would like to thank T. Abukawa for helpful discussions of the α -FeSi₂ phase.

- *Present address: Toyota Central R&D Labs., Inc., Nagakute, Aichi 480-1192, Japan. Electronic address: e1354@mosk.tytlabs.co.jp
- †Corresponding author. Electronic address: khattori@ms.naist.jp
- ¹D. Leong, M. Harry, K. J. Reeson, and K. P. Homewood, *Nature (London)* **387**, 686 (1997).
 - ²T. Suemasu, Y. Negishi, K. Takakura, and F. Hasegawa, *Jpn. J. Appl. Phys., Part 2* **39**, L1013 (2000).
 - ³K. Radermacher, A. Schüppen, and S. Mantl, *Solid-State Electron.* **37**, 443 (1994).
 - ⁴N. G. Galkin, D. L. Goroshko, S. Ts. Krivoshchapov, and E. S. Zakharova, *Appl. Surf. Sci.* **175-176**, 230 (2001).
 - ⁵D. Berling, G. Gewinner, M. C. Hanf, K. Hricovini, S. Hong, B. Loegel, A. Mehdaoui, C. Pirri, M. H. Tuilier, and P. Wetzal, *J. Magn. Magn. Mater.* **191**, 331 (1999).
 - ⁶Y. Takagi, A. Nishimura, A. Nagashima, and J. Yoshino, *Surf. Sci.* **514**, 167 (2002).
 - ⁷A. N. Hattori, K. Hattori, K. Kataoka, and H. Daimon (unpublished).
 - ⁸K. Hattori, T. Nishimura, K. Kataoka, Y. Shimamoto, and H. Daimon, *Thin Solid Films* **464-465**, 5 (2004).
 - ⁹P. Rygus, P.-R. Steiner, and H. Froitzheim, *Surf. Sci.* **352-354**, 523 (1996).
 - ¹⁰M. Hansen and K. Anderko, *Constitution of Binary Alloys* (McGraw-Hill, New York, 1958).
 - ¹¹O. Kubaschewski, *Iron-Binary Phase Diagrams* (Springer, Berlin, 1982).
 - ¹²P. Villars and L. D. Calvert, *Person's Handbook of Crystallographic Data for Intermetallic Phases* (ASM International, Metals Park, OH, 1991).
 - ¹³S. Walter, F. Blobner, M. Krause, S. Müller, K. Heinz, and U. Starke, *J. Phys.: Condens. Matter* **15**, 5207 (2003).
 - ¹⁴W. Weiß, M. Kutschera, U. Starke, M. Mozaffari, K. Reshöft, U. Köhler, and K. Heinz, *Surf. Sci.* **377-379**, 861 (1997).
 - ¹⁵H. von Känel, K. A. Mäder, E. Müller, N. Onda, and H. Sirringhaus, *Phys. Rev. B* **45**, 13807 (1992).
 - ¹⁶S. Walter, R. Bandorf, W. Weiss, K. Heinz, U. Starke, M. Strass, M. Bockstedte, and O. Pankratov, *Phys. Rev. B* **67**, 085413 (2003).
 - ¹⁷U. Starke, W. Weiss, M. Kutschera, R. Bandorf, and K. Heinz, *J. Appl. Phys.* **91**, 6154 (2002).
 - ¹⁸J. Chevrier, V. Le Thanh, S. Nitsche, and J. Derrien, *Appl. Surf. Sci.* **56-58**, 438 (1992).
 - ¹⁹A. L. Vazquez de Parga, J. de la Figuera, C. Ocal, and R. Miranda, *Ultramicroscopy* **42-44**, 845 (1992).
 - ²⁰W. Raunau, H. Niehus, T. Schilling, and G. Comsa, *Surf. Sci.* **286**, 203 (1993).
 - ²¹U. Kafader, C. Pirri, P. Wetzal, and G. Gewinner, *Appl. Surf. Sci.* **64**, 297 (1993).
 - ²²X. Wallart, J. P. Nys, and C. Tételin, *Phys. Rev. B* **49**, 5714 (1994).
 - ²³N. Motta, A. Sgarlata, G. Gaggiotti, F. Patella, A. Balzarotti, and M. De Crescenzi, *Surf. Sci.* **284**, 257 (1993).
 - ²⁴A. Wawro, S. Suto, R. Czajka, and A. Kasuya, *Phys. Rev. B* **67**, 195401 (2003).
 - ²⁵S. Hajjar, G. Garreau, S. Pelletier, D. Bolmont, and C. Pirri, *Phys. Rev. B* **68**, 033302 (2003).
 - ²⁶M. Krause, F. Blobner, L. Hammer, K. Heinz, and U. Starke, *Phys. Rev. B* **68**, 125306 (2003).
 - ²⁷Y. L. Gavriljuk, L. Y. Kachanova, and V. G. Lifshits, *Surf. Sci. Lett.* **256**, L589 (1991).
 - ²⁸N. Jedrecy, Y. Zheng, A. Waldhauer, M. Sauvage-Simkin, and R. Pinchaux, *Phys. Rev. B* **48**, 8801 (1993).
 - ²⁹N. Jedrecy, A. Waldhauer, M. Sauvage-Simkin, R. Pinchaux, and Y. Zheng, *Phys. Rev. B* **49**, 4725 (1994).
 - ³⁰N. Cherief, R. Cinti, M. de Crescenzi, J. Derrien, T. A. Nguyen Tan, and J. Y. Veuillen, *Appl. Surf. Sci.* **41/42**, 241 (1989).
 - ³¹N. Cherief, C. D'Anterrosches, R. C. Cinti, T. A. Nguyen Tan, and J. Derrien, *Appl. Phys. Lett.* **55**, 1671 (1989).
 - ³²A. L. Vázquez de Parga, J. de la Figuera, J. E. Prieto, C. Ocal, and R. Miranda, *Appl. Phys. A: Solids Surf.* **57**, 477 (1993).
 - ³³J. Derrien, J. Chevrier, Le Thanh Vinh, I. Berbezier, C. Giannini, S. Lagomarsino, and M. G. Grimaldi, *Appl. Surf. Sci.* **73**, 90 (1993).
 - ³⁴R. Tsushima, Y. Michishita, S. Fujii, H. Okado, K. Umezawa, Y. Maeda, Y. Terai, K. Oura, and M. Katayama, *Surf. Sci.* **579**, 73 (2005).
 - ³⁵A. Rizzi, H. Moritz, and H. Lüth, *J. Vac. Sci. Technol. A* **9**, 912 (1991).
 - ³⁶T. Urano, T. Ogawa, T. Kanaji, and F. Fujimoto, *J. Vac. Sci. Technol. A* **5**, 2046 (1987).
 - ³⁷J. Alvarez, A. L. Vázquez de Parga, J. J. Hinarejos, J. de la Figuera, E. G. Michel, C. Ocal, and R. Miranda, *Phys. Rev. B* **47**, 16048 (1993).
 - ³⁸K. Kataoka, F. Matsui, Y. Kato, F. Z. Guo, T. Matsushita, K. Hattori, and H. Daimon, *Surf. Rev. Lett.* (to be published).
 - ³⁹N. Minami, D. Makino, T. Matsumura, C. Egawa, T. Sato, K. Ota, and S. Ino, *Surf. Sci.* **514**, 211 (2002).
 - ⁴⁰H. Sirringhaus, N. Onda, E. Müller-Gubler, P. Müller, R. Stalder, and H. von Känel, *Phys. Rev. B* **47**, 10567 (1993).
 - ⁴¹H. Daimon and S. Ino, *Surf. Sci.* **164**, 320 (1985).
 - ⁴²T. Sakurai and H. D. Hagstrum, *Phys. Rev. B* **12**, 5349 (1975).
 - ⁴³K. Mortensen, D. M. Chen, P. J. Bedrossian, J. A. Golovchenko, and F. Besenbacher, *Phys. Rev. B* **43**, 1816 (1991).
 - ⁴⁴O. Romanyuk, K. Kataoka, F. Matsui, K. Hattori, and H. Daimon, *Czech. J. Phys.* **56**, 267 (2006).
 - ⁴⁵Y. Dusausoy, J. Protas, R. Wandji, and B. Roques, *Acta Crystallogr., Sect. B: Struct. Crystallogr. Cryst. Chem.* **27**, 1209 (1971).
 - ⁴⁶E. G. Moroni, W. Wolf, J. Hafner, and R. Podloucky, *Phys. Rev. B* **59**, 12860 (1999).